Structural insights into human propionyl-CoA carboxylase (PCC) and 3-methylcrotonyl-CoA carboxylase (MCC)

Fayang Zhou[1,2,3,4]†, Yuanyuan Zhang[3]†, Yuyao Zhu[2,4], Qiang Zhou[3], Yigong Shi[3], Qi Hu[2,4]*

[1]College of Life Sciences, Zhejiang University; Hangzhou 310058, China.

[2]School of Life Sciences, Westlake University; Hangzhou 310024, China.

[3]Zhejiang Key Laboratory of Structural Biology, School of Life Sciences, Westlake University; Hangzhou 310024, China.

[4]Westlake AI Therapeutics Lab, Westlake Laboratory of Life Sciences and Biomedicine; Hangzhou 310058, China.

*Corresponding author. Email: huqi@westlake.edu.cn

†These authors contributed equally to this work.

Abstract

Propionyl-CoA carboxylase (PCC) and 3-methylcrotonyl-CoA carboxylase (MCC) are biotin-dependent carboxylases (BDCs) that catalyze the metabolism of odd-chain fatty acids, cholesterol, and specific amino acids. For human PCC and MCC, only a low-resolution (15 Å) three-dimensional structure of human PCC has been reported. Here, we report high-resolution (2.29–3.28 Å) cryo-EM structures of human PCC and MCC holoenzymes in their apo and acetyl-CoA and propionyl-CoA-bound states. Propionyl-CoA and acetyl-CoA bind to PCC with almost identical binding modes, indicating that the acyl-CoA specificity of PCC is largely attributed to minor differences in interactions mediated by the acyl groups. In MCC, biotin is relocated from an exo-site to an endo-site upon acetyl-CoA binding, suggesting coordination between biotin binding and acyl-CoA binding. Our work provides insights into the substrate specificity and catalytic process of BDCs.

Introduction

Biotin-dependent carboxylases (BDCs) catalyze the carboxylation of several key metabolites using covalently linked biotin as a cofactor(*1, 2*). In humans, there are four types of BDCs: acetyl-CoA carboxylase (ACC), propionyl-CoA carboxylase (PCC), 3-methylcrotonyl-CoA carboxylase (MCC), and pyruvate carboxylase (PYC)(*1, 2*). All BDCs contain a biotin carboxylase (BC) domain, a carboxyltransferase (CT) domain, and a biotin carboxyl carrier protein (BCCP) domain(*1, 2*). The carboxylation reaction involves a two-step process(*1, 2*). Firstly, the biotin covalently linked to the BCCP domain is carboxylated in the BC domain, using bicarbonate as the donor of the carboxyl group(*3*). Secondly, the carboxylated biotin is carried to the CT domain by the BCCP domain(*4*). In the CT domain, the carboxyl group is transferred from the biotin to acetyl-CoA, propionyl-CoA, 3-methylcrotonyl-CoA, or pyruvate(*2, 5*). Among the four human BDCs, ACC and PYC each consist of a single chain that incorporates the BC, CT, and BCCP domains(*2*). In contrast, PCC and MCC have their BC, CT, and BCCP domains divided into two chains: the α subunits contain the BC and BCCP domains, with an intermediate BC-CT interaction (BT) domain between them, while the β subunits solely consist of the CT domain(*2*).

In humans, PCC and MCC catalyze the carboxylation of propionyl-CoA and 3-methylcrotonyl-CoA (MC-CoA), respectively(*6, 7*). Propionyl-CoA is an intermediate in the metabolism of odd-chain fatty acids, cholesterol, and amino acids including valine, isoleucine, methionine, and threonine; its carboxylated product (S)-methylmalonyl-CoA is then converted into succinyl-CoA and subsequently metabolized in the tricarboxylic acid cycle(*6*). MC-CoA is an intermediate in the metabolism of leucine; following carboxylation, the resulting product 3-methylglutaconyl-CoA (MG-CoA) is further converted into 3-hydroxy-3-methylglutaryl-CoA (HMG-CoA) and then involved in the synthesis of cholesterol(*8*). Therefore, both PCC and MCC play important roles in metabolic processes. Loss-of-function mutations in MCC and PCC lead to severe metabolic disorders(*6, 9-11*).

The protein sequences and functions of PCC and MCC are conserved from bacteria to humans. A crystal structure of a chimeric bacteria PCC holoenzyme, obtained by co-expressing the α subunit of *Ruegeria pomeroyi* PCC (RpPCC) with the β subunit of *Roseobacter denitrificans* PCC (RdPCC) in *E. coli*, was determined at a resolution of 3.2 Å (*12*). The PCC holoenzyme is a dodecamer formed by six α subunits and six β subunits, thereby referred to as the $\alpha_6\beta_6$ holoenzyme(*12*). Crystal structures of a bacteria MCC (*Pseudomonas aeruginosa* MCC, PaMCC) holoenzyme reveal that the MCC holoenzyme is also a $\alpha_6\beta_6$ dodecamer(*13*). The structures of bacteria PCC and MCC holoenzymes reveal how the α subunits and β subunits assemble to form the holoenzymes(*12, 13*). However, our understanding of human PCC and MCC is constrained by the limited availability of high-resolution three-dimensional structures. Thus far, only a low-resolution cryo-EM structure of human PCC holoenzyme (15 Å) has been reported (*12*), highlighting the need for high-resolution structural information of human PCC and MCC.

In this study, we purified the endogenous PCC and MCC from human cells and determined the cryo-EM structures of human PCC and MCC holoenzymes in the apo (PCC or MCC holoenzyme alone), acetyl-CoA-bound, and propionyl-CoA-bound states, at resolutions ranging from 2.29 to 3.28 Å. Structural analysis reveals that human PCC and MCC holoenzymes have overall structures similar to their bacterial homologs. For human PCC holoenzyme, the structure in the acetyl-CoA-bound state closely resembles the structures in the apo and the propionyl-CoA-bound state. In these structures, the covalently linked biotin binds to a site that is distant from the catalytic residues in the CT domain, rendering it catalytically incompetent. In contrast, for human MCC holoenzyme, acetyl-CoA binding, but not propionyl-CoA binding, induces conformational

78 changes in the acyl-CoA binding pocket, thus relocating the covalently linked biotin from an exo-
79 site to an endo-site that is closer to the catalytic residues in the CT domain.

80

81 **Results**

82 ***Overall structures of human PCC and MCC holoenzymes***

83 The BDCs endogenously expressed in Expi 293F cells were purified using streptavidin beads (the
84 Strep-Tactin®XT resin) since streptavidin can specifically bind to the covalently linked biotin in
85 the BDCs. The purified BDCs were further purified using size exclusion chromatography. Mass
86 spectrometry analysis identified all four types of human BDCs in the purified samples (fig. S1).
87 The samples were subjected to cryo-EM sample preparation (fig. S1, A to C).

88 The cryo-EM structures of the PCC and MCC holoenzymes alone, referred to as PCC-apo
89 and MCC-apo, were determined at resolutions of 3.02 Å and 2.29 Å, respectively (figs. S2A, S3, A
90 to D and S4, A to D, tables S1 and S2). The cryo-EM maps have good quality to support model
91 building (figs. S5, S6 and S7).

92 Both the PCC and MCC holoenzymes consist of six α subunits and six β subunits. The cryo-
93 EM densities of one PCCα subunit in the PCC-ACO structure and three MCCα subunits in the
94 MCC-apo, MCC-ACO, and MCC-PCO structures are partially missing. Therefore, in order to
95 demonstrate the complete structures of the holoenzymes, these subunits were built into the
96 structures based on the density of the BT domain in each α subunit (fig. S8). The $\alpha_6\beta_6$ dodecamer
97 can be divided into four layers. The six β subunits are stacked into two layers to form the core of
98 the holoenzymes, with three β subunits laid head to end in each layer (Fig. 1, A and B). The six α
99 subunits are separated into two layers and situated at the top and bottom sides of the β subunit core,
100 with each layer contains three α subunits. A major difference between the PCC and MCC
101 holoenzymes is that the three α subunits in each layer have no contact in the PCC holoenzyme but
102 interact with each other in the MCC holoenzyme (Fig. 1, A and B).

103 The overall structures of human PCC and MCC holoenzymes are similar to the reported
104 crystal structures of bacteria PCC and MCC holoenzymes, respectively (Fig. 1, C and D).
105 Specifically, alignment of the β subunits in the PCC-apo structure with those in the structure of a
106 chimeric bacteria PCC holoenzyme (PDB code: 3N6R) shows that the β subunit cores in the two
107 structures are very similar(*12*). Each α subunit in human PCC holoenzyme has a minor rotation
108 relative to the corresponding α subunit in the bacteria PCC holoenzyme (Fig. 1C). Similarly, the β
109 subunit core in the MCC-apo structure aligns well with that in the crystal structure of a bacteria
110 MCC holoenzyme (PDB code: 3U9T), with each α subunit slightly rotated in comparison to the
111 corresponding α subunit in the bacteria MCC holoenzyme(*13*) (Fig. 1D). The structures of the BC,
112 BT, and BCCP domains in the α subunits of human PCC and MCC resemble the corresponding
113 domains in bacteria PCC and MCC(*12, 13*), except that the BT domain of human MCC has one
114 more β strand in comparison to that of the PaMCC (fig. S9).

115 ***Organization of the catalytic domains in human PCC and MCC holoenzymes***

116 We incubated the purified human BDCs with propionyl-CoA (fig. S1, D to G), which is the
117 substrate of PCC, and determined the cryo-EM structures of the propionyl-CoA-bound PCC and
118 MCC holoenzymes (referred to as PCC-PCO and MCC-PCO), at resolutions of 2.80 Å and 2.36 Å,
119 respectively (figs. S2B, S3, E to H, S4, E to H, S6 and S7, tables S1 and S2). The two structures
120 are almost identical to the structures of PCC-apo and MCC-apo, respectively. Although bicarbonate,
121 $MgCl_2$, and ATP were added to the purified BDC samples to facilitate the carboxylation reaction,

122 the cryo-EM density of the biotin region does not provide conclusive evidence as to whether the
123 covalently linked biotin in the PCC holoenzyme structures was indeed carboxylated. Thus, the cryo-
124 EM structures only contain the uncarboxylated biotin.

125 The two-step carboxylation reactions catalyzed by PCC and MCC require the coordination
126 of the BC, BCCP domains in the α subunit and the CT domain in the β subunit (Fig. 2A). In human
127 PCC holoenzyme, each α subunit binds to one β subunit containing the CT domain that can be
128 divided into CT-N and CT-C subdomains (Fig. 2B). The BC domain in the α subunit is situated on
129 the CT-C subdomain, while the BCCP domain also attaches to the CT-C subdomain and positions
130 the covalently linked biotin to a pocket adjacent to the propionyl-CoA binding pocket. The BT
131 domain tightly interacts with both the CT-N and CT-C subdomains and functions as a hub to hold
132 the BC and BCCP domains together with the CT domain (Fig. 2B).

133 In contrast, in human MCC holoenzyme, each α subunit binds to two β subunits (referred to
134 as β1 and β2) (Fig. 2C). The CT-N subdomain of β1 interacts with the CT-C subdomain of β2. The
135 BT domain of the α subunit associates with both the CT-N and CT-C subdomains of β1, while the
136 BCCP domain attaches to the CT-C subdomain of β2. The propionyl-CoA binds to a pocket formed
137 by the CT-C of β2 and the CT-N of a third β subunit (β3) from the other β subunit layer. The BC
138 domain has no contact with the β subunits.

139 The variances in the organization of the catalytic domains in the PCC holoenzyme and the
140 MCC holoenzyme are partly attributed to the distinct arrangement of their CT domains (Fig. 2D).
141 Alignment of the CT-N subdomains shows that the CT-C subdomains in PCC and MCC have
142 distinct orientations (Fig. 2D). The CT domain in PCC can perfectly align with a combination
143 including the CT-N of β1 and the CT-C of β2 of MCC (Fig. 2E).

144 ***Propionyl-CoA binding in human PCC holoenzyme***

145 In each PCC holoenzyme, six propionyl-CoA molecules are observed binding to the six active sites
146 of CT domains. Each binding site for propionyl-CoA is formed by the CT-C subdomain of one β
147 subunit and the CT-N subdomain of another β subunit in the other layer (Fig. 3A). The conformation
148 of the propionyl-CoA binding pocket in the PCC-PCO structure is only slightly different from that
149 in the PCC-apo structure (Fig. 3B). The AMKM motif in the BCCP domain and the biotin
150 covalently linked to it also show only minor conformational differences in the PCC-PCO structure
151 compared to the PCC-apo structure (Fig. 3C). The distances between the ureido ring carbonyl
152 oxygen of the biotin and the main chain amide of the catalytic residues G437 and A438 in the
153 corresponding CT domain in the PCC-PCO structure are more than 7 Å, which is too far for an
154 efficient catalytic process (Fig. 3C). This finding suggests that the biotin may need to relocate to a
155 site that is closer to the catalytic residues to facilitate the carboxylation reaction.

156 Before our study, two structures were reported to demonstrate the binding of CoA or
157 propionyl-CoA in the CT domains of bacteria PCCs. One is the crystal structure of the β subunits
158 of *Streptomyces coelicolor* PCC (ScPCC) in complex with propionyl-CoA (PDB code: 1XNY)(*14*).
159 The other is the cryo-EM structure of the *Methylorubrum extorquens* PCC (MePCC) holoenzyme
160 in complex with CoA (PDB code: 6YBP)(*15*). The binding mode of propionyl-CoA in our PCC-
161 PCO structure is distinct from that in the ScPCC β subunit structure, but similar to that in the
162 MePCC holoenzyme structure (Fig. 3D, E).

163 ***Acetyl-CoA binding in human PCC and MCC holoenzymes***

In an unpublished manuscript (Zhou *et al*, 2024), we incubated the purified human BDCs with acetyl-CoA, which is a substrate of ACC, and determined the cryo-EM structure of the acetyl-CoA-bound ACC. Using the same batch of purified BDCs (fig. S1, H to K), we also determined the cryo-EM structures of human PCC and MCC holoenzymes in the acetyl-CoA-bound state (referred to as PCC-ACO and MCC-ACO) at resolutions of 3.38 Å and 2.85 Å, respectively (figs. S2C, S3, I to L, S4, I to L, S6 and S7, tables S1 and S2).

The PCC-ACO structure closely resembles the PCC-apo and the PCC-PCO structures. The acetyl-CoA in the PCC-ACO structure has a binding mode similar to the propionyl-CoA in the PCC-PCO structure (Fig. 3F). The conformation of the acyl-CoA binding pocket in both structures is also highly similar (Fig. 3F). It was reported that D422 in the β subunit of a bacteria PCC (ScPCC) is crucial for the substrate specificity of ScPCC, and the D422I mutation significantly increased the catalytic activity of ScPCC towards acetyl-CoA(*14, 16*). But the PCC-PCO structure shows that D440, which corresponds to D422 in the β subunit of ScPCC, is not directly involved in the interaction with propionyl-CoA or acetyl-CoA (Fig. 3F).

The overall structure of MCC-ACO is also similar to that of MCC-apo, but alignment of the CT-N subdomains shows that the position of the BCCP domain and the conformation of the acyl-CoA binding pocket in the MCC-ACO structure are significantly different from those in the MCC-apo structure (Fig. 4A). Specifically, the BCCP domain moves towards the CT-C subdomain in the MCC-ACO structure compared to that in the MCC-apo structure (Fig. 4A). Consequently, the covalently linked biotin moves from an exo-site to an endo-site that is deeper in the pocket formed by the CT-N and CT-C subdomains from two β subunits (Fig. 4B). At the exo-site, the ureido ring carbonyl oxygen of the biotin is about 8 Å away from the main chain amide of the catalytic residues G437 and A438 (fig. S10A). In contrast, at the endo-site, the distance is shortened to about 3.5 Å (fig. S10B). The acyl-CoA binding pocket, also formed by the CT-N and CT-C subdomains from two β subunits, switches from an open conformation in the MCC-apo structure to a closed conformation in the MCC-ACO structure (Fig. 4, C to E), with the major conformational change occurring at two helices (residues 474 to 517) in the CT-C subdomain and one helix (residues 243 to 252) in the CT-N subdomain (Fig. 4C).

We aligned the MCC-ACO structure with the crystal structure of a bacteria MCC (PaMCC) holoenzyme in complex with CoA (PDB code: 3U9S) and observed a high similarity between them(*13*). Both the BCCP domain and the CT domain in the MCC-ACO structure align well with those in the PaMCC structure. The AMKM motif and biotin in the two structures also show a high similarity (Fig. 4F). Interestingly, alignment of the CoA-bound PaMCC holoenzyme structure with the structure of the PaMCC holoenzyme alone shows a change in the conformation of two helices in the CT-C subdomain of PaMCC(*13*), similar to that observed in the alignment of the MCC-ACO structure with the MCC-apo structure (Fig. 4C). These findings suggest that conformational changes in the acyl-CoA binding pocket, combined with the change in the position of the BCCP domain, may be necessary for the catalytic process of MCC.

Discussion

Several three-dimensional structures of PCCs and MCCs have been reported (*12-18*), however, most of them are from bacteria and expressed in *E. coli(12-16)*. In our study, we extracted the endogenous PCC and MCC from human cells by one-step affinity purification (fig. S1) and determined their cryo-EM structures in the apo and substrate-bound states. The overall structures of human PCC and MCC holoenzymes resemble those of their bacterial homologs. This similarity

209 aligns with the conserved functions of PCCs and MCCs across species, ranging from prokaryotes
210 to eukaryotes.

211 A previous study showed that PCC purified from human liver also catalyzed the
212 carboxylation of acetyl-CoA, but the rate was only about 1.5% of that observed for propionyl-
213 CoA(*19*). Propionyl-CoA and acetyl-CoA, which have highly similar structures, undergo
214 carboxylation at analogous positions—the α carbon of the propionyl or the acetyl group. A key
215 question is, what determines the substrate specificity of the PCC holoenzyme? The PCC-PCO and
216 PCC-ACO structures determined in our study demonstrate that both propionyl-CoA and acetyl-
217 CoA can bind to human PCC holoenzyme, with a similar binding mode (Fig. 3F). Thus, the
218 selectivity of PCC towards propionyl-CoA and acetyl-CoA is largely determined by the interactions
219 between the acyl group and PCC. The longer acyl group in propionyl-CoA, in comparison to that
220 in acetyl-CoA, may mediate a stronger hydrophobic interaction that stabilizes the α carbon of the
221 acyl group at a proper position to react with the carboxylated biotin.

222 The cryo-EM structures of MCC-apo and MCC-ACO reveal that there are two distinct
223 binding sites in the CT domains of human MCC holoenzyme for the covalently linked biotin (Fig.
224 4B). In the MCC-apo structure, the biotin binds to a site that is distant from the catalytic residues
225 A447 and G448, thus referred to as the exo-site; while in the MCC-ACO structure, the biotin binds
226 to a site that is closer to A447 and G448 and is therefore referred to as the endo-site (Fig. 4B, fig.
227 S10). Binding of acetyl-CoA to the acyl-CoA binding pocket of the CT domains induces
228 conformational changes in these domains, leading to the relocation of the biotin molecule from the
229 exo-site to the endo-site. Conformational changes in the CT domains upon CoA binding were also
230 observed in the crystal structures of PaMCC(*13*). These findings indicate a coordination between
231 biotin binding and acetyl-CoA binding for the MCC holoenzymes. It should be noted that acetyl-
232 CoA is not a substrate for MCC. Next, we will try to determine the cryo-EM structure of human
233 MCC in complex with its substrate MC-CoA to see whether the binding of MC-CoA to MCC has
234 similar effects to the binding of acetyl-CoA.

235 Similarly, in an unpublished manuscript (Zhou *et al*., 2024), it was also observed that the
236 covalently linked biotin in the ACC-citrate filament, which is the active form of human ACC, binds
237 to an exo-site that is distant from the acetyl-CoA binding site in the absence of acetyl-CoA. In
238 contrast, in the crystal structure of CoA-bound yeast ACC, the biotin occupies an endo-site that is
239 closer to the acetyl-CoA binding site(*20*).

240 In the crystal structure of *Staphylococcus aureus* PYC (SaPYC), two distinct binding sites
241 for the covalently linked biotin were also observed, one is about 20 Å from the active site of the CT
242 domain and is called the exo site, and the other is in the active site of the CT domain(*1, 21*).

243 Taken together, our studies, combined with previous research, suggest that the presence of
244 an exo-site and an endo-site for the binding of covalently linked biotin is a common feature shared
245 by many BDCs. The transfer of biotin from the exo-site to the endo-site may be promoted by the
246 coordinated binding of acyl-CoA or pyruvate to the CT domains. Conversely, relocation of biotin
247 from the endo-site to the exo-site might facilitate the release of the products after the second step
248 carboxylation reaction.

249 However, we did not observe the relocation of biotin to an endo-site upon acyl-CoA binding
250 in human PCC holoenzyme (Fig. 3). Additionally, while we did observe relocation of biotin and
251 conformational changes in the CT domains of human MCC holoenzyme upon binding with acetyl-
252 CoA, similar changes were not observed with propionyl-CoA binding. Further studies focusing on

253 capturing the structures of human PCC and MCC holoenzymes in various states during their
254 catalytic processes would contribute to a comprehensive understanding of the underlying catalytic
255 mechanisms.

256

257 **Materials and Methods**

258 ***Cell culture***

259 Expi 293F cells (Thermo Scientific) were cultured in SMM 293T-II medium (Sino Biological) at
260 37 °C with 5% CO_2 in a Multitron-Pro incubator (Infors). After the density reached 2.0×10^6/mL,
261 the cells were cultured for an additional 48 h, then harvested by centrifuging at 4,000 ×*g* (Fiberlite
262 F9-6×1000 LEX rotor, Thermo Scientific) for 10 min and resuspended with HBS buffer (20 mM
263 HEPES, pH 7.4, 150 mM NaCl). The cells were snap frozen and stored at −80 °C.

264 ***Endogenous purification of biotin dependent carboxylases***

265 The frozen cells were thawed and disrupted using a high-pressure cell crusher and centrifuged at
266 23,376 ×*g* (JA-14.50 rotor, Beckman) for 1 h at 4 °C. The supernatant was incubated with Strep-
267 Tactin®XT resin (IBA Lifesciences) for 1 h at 4 °C and then washed with HBS buffer. The proteins
268 were eluted by HBS buffer supplemented with 50 mM *D*-biotin (J&K Scientific) and further purified
269 by size-exclusion chromatography (Superose 6 Increase 10/300 GL column, Cytiva) using HBS as
270 the running buffer. Different batches of proteins were purified for the preparation of the samples at
271 different substrate binding states. For the substrate-free sample (the apo sample), fractions eluted
272 within 12.5–15 mL were combined and concentrated to 2.85 mg/mL. For the substrate-bound
273 samples, fractions eluted within 12.5–16.5 mL were combined and concentrated to 2.5–2.65 mg/mL.
274 The samples were pre-incubated with 25 mM $NaHCO_3$, 10 mM $MgCl_2$ and 10 mM propionyl-CoA
275 for the propionyl-CoA-bound sample (the PCO sample) or acetyl-CoA for the acetyl-CoA-bound
276 sample (the ACO sample), followed by adding 10 mM ATP immediately before frozen on the cryo-
277 EM grids. The proteins were analyzed by mass spectrometry and applied for cryo-EM grids
278 preparation the same day purified.

279 ***Cryo-EM data acquisition and pre-processing***

280 Holey grids (Holey carbon filmed 300 mesh gold grids, R1.2/1.3, Quantifoil) were glow discharged
281 with a medium RF power for 30 s using a plasma cleaner PDC-32G-2 (Harrick Plasma) prior use.
282 Aliquots (4 μL) of each sample were loaded to the grids and flash frozen in liquid ethane
283 immediately using Vitrobot Mark IV (Thermo Fisher Scientific). The cryo-EM grids were stored
284 in liquid nitrogen until data acquisition.

285 The cryo-EM grids were transferred to a Titan Krios TEM (FEI) operating at 300 kV
286 equipped with a K3 Summit direct electron detector (Gatan) and a GIF Quantum energy filter
287 (Gatan). Zero-loss movie stacks were automatically collected using EPU software (FEI) with a slit
288 width of 20 eV on the energy filter and a defocus range from −1.2 to −2.2 μm in super-resolution
289 mode at an 81,000× nominal magnification. Each movie stack, which contained 32 frames, was
290 exposed for 2.56 s with a total electron dose of ~50 $e^-/Å^2$. The stacks were motion corrected using
291 MotionCor2 with a binning factor of 2, resulting in the pixel size of 1.0773 Å(*22*). Dose weighting
292 was performed concurrently(*23*). The movie stacks were imported to cryoSPARC (v3.3.2, Structura
293 Biotechnology) for CTF estimation and downstream processing(*24*).

294 ***Data processing***

For the apo sample, 11,481 micrographs were captured and imported to cryoSPARC for processing. Particles were automatically picked according to the templates generated from an initial 2D classification of the manually picked particles and extracted with a box size of 488 pixels for *ab-initio* reconstruction and heterogeneous refinement jobs, yielding the maps of PCC (11.5%) and MCC (37.6%) holoenzymes. To get the high-resolution map of PCC holoenzyme, a non-uniform refinement with the corresponding group of particles was carried out, yielding a detailed map, yet the density for one of the α subunits was lacking. To solve this problem, distinct reference volumes with (Ref-A) or without (Ref-B) the corresponding PCCα were generated by UCSF Chimera (v1.16)(*25*). After a refinement based on multiple references, 61,567 particles were subjected to the homogenous refinement, yielding the complete map of PCC (PCC-apo) at 3.02 Å resolution. For the case of MCC holoenzyme, a round of non-uniform refinement was carried out. After that, the volume chirality was flipped, and the map was further polished by a series of refinement jobs, resulting in the map of MCC (MCC-apo) at 2.29 Å resolution.

For the PCO sample, 10,898 micrographs were imported for data processing. After particle picking, extraction (box size = 488 pixels), *ab-initio* reconstruction and heterogeneous refinement, the PCC (8.7%) and MCC (39.7%) representing volumes were further processed by non-uniform refinement, yielding the maps generated from 105,293 and 476,773 particles, respectively. The PCC map was subjected to local CTF refinement and subsequent local refinement, yielding the final map of propionyl-CoA bound PCC holoenzyme (PCC-PCO) at 2.80 Å. The MCC map was further polished by heterogenous refinement and non-uniform refinement after flipping chirality, producing the final map of propionyl-CoA bound MCC holoenzyme (MCC-PCO) at 2.36 Å.

For the ACO sample, 4,036 micrographs were collected and imported. Particle picking, extraction (box size = 488 pixels), initial 2D classification and particle clustering jobs were carried out accordingly. 31,622 PCC-like particles were enriched in cluster-A and subsequently subjected to *ab-initio* reconstruction and non-uniform refinement. After flipping the volume chirality, the refined map was further polished by another round of non-uniform refinement, yielding the 3.38 Å map of acetyl-CoA bound PCC holoenzyme (PCC-ACO). In cluster-B, 273,428 MCC-like particles were enriched. These particles were *ab-initio* reconstructed and classified to 4 volumes, of which one, composed of 39.9% of particles, exhibited clear secondary structure features of MCC. This map was further processed by heterogeneous refinement and non-uniform refinement jobs, yielding the final map of acetyl-CoA bound MCC holoenzyme (MCC-ACO) at 2.85 Å resolution.

The resolutions mentioned above were determined according to the gold-standard Fourier shell correlation 0.143 criterion and with a high-resolution noise substitution method(*26*). All the reconstructed maps were subjected to further model building.

Model building and structure refinement

The AlphaFold predicted structures were used as the templates for the model building of PCC and MCC holoenzymes(*27, 28*). The reference models were automatically placed in the EM maps using Rosetta and manually adjusted using Coot, resulting the modified models(*29, 30*). Each residue was manually checked with the chemical properties taken into consideration during model building. Several segments, whose corresponding densities were invisible, were not modeled. Real space refinement was performed using Phenix with secondary structure and geometry restraints to prevent overfitting(*31*). For the cross-validation of the structure, the model was refined against one of the two independent half maps from the gold-standard 3D refinement approach. Then, the refined model was tested against the other half map. Statistics associated with data collection, 3D reconstruction and model building were summarized in tables S1 and S2.

References

1. L. Tong, Structure and function of biotin-dependent carboxylases. *Cell Mol Life Sci* **70**, 863-891 (2013).
2. L. Tong, in *Adv Protein Chem Struct Biol*. (2017), vol. 109, pp. 161-194.
3. J. B. Thoden, C. Z. Blanchard, H. M. Holden, G. L. Waldrop, Movement of the biotin carboxylase B-domain as a result of ATP binding. *J Biol Chem* **275**, 16183-16190 (2000).
4. X. Yao, C. Soden, Jr., M. F. Summers, D. Beckett, Comparison of the backbone dynamics of the apo- and holo-carboxy-terminal domain of the biotin carboxyl carrier subunit of Escherichia coli acetyl-CoA carboxylase. *Protein Sci* **8**, 307-317 (1999).
5. J. Lombard, D. Moreira, Early evolution of the biotin-dependent carboxylase family. *BMC Evol Biol* **11**, 232 (2011).
6. P. Wongkittichote, N. Ah Mew, K. A. Chapman, Propionyl-CoA carboxylase - A review. *Mol Genet Metab* **122**, 145-152 (2017).
7. C. H. Chu, D. Cheng, Expression, purification, characterization of human 3-methylcrotonyl-CoA carboxylase (MCCC). *Protein Expr Purif* **53**, 421-427 (2007).
8. S. L. Nissen, N. N. Abumrad, Nutritional role of the leucine metabolite β-hydroxy β-methylbutyrate (HMB). *The Journal of Nutritional Biochemistry* **8**, 300-311 (1997).
9. D. Ballhausen, L. Mittaz, O. Boulat, L. Bonafe, O. Braissant, Evidence for catabolic pathway of propionate metabolism in CNS: expression pattern of methylmalonyl-CoA mutase and propionyl-CoA carboxylase alpha-subunit in developing and adult rat brain. *Neuroscience* **164**, 578-587 (2009).
10. H. Fonseca *et al.*, 3-Methylcrotonyl-CoA carboxylase deficiency: Mutational spectrum derived from comprehensive newborn screening. *Gene* **594**, 203-210 (2016).
11. M. F. Dantas *et al.*, 3-Methylcrotonyl-CoA carboxylase deficiency: mutation analysis in 28 probands, 9 symptomatic and 19 detected by newborn screening. *Hum Mutat* **26**, 164 (2005).
12. C. S. Huang *et al.*, Crystal structure of the $\alpha_6\beta_6$ holoenzyme of propionyl-coenzyme A carboxylase. *Nature* **466**, 1001-1005 (2010).
13. C. S. Huang, P. Ge, Z. H. Zhou, L. Tong, An unanticipated architecture of the 750-kDa alpha6beta6 holoenzyme of 3-methylcrotonyl-CoA carboxylase. *Nature* **481**, 219-223 (2011).
14. L. Diacovich *et al.*, Crystal structure of the beta-subunit of acyl-CoA carboxylase: structure-based engineering of substrate specificity. *Biochemistry* **43**, 14027-14036 (2004).
15. M. Scheffen *et al.*, A new-to-nature carboxylation module to improve natural and synthetic CO2 fixation. *Nat Catal* **4**, 105-115 (2021).
16. A. Arabolaza *et al.*, Crystal structures and mutational analyses of acyl-CoA carboxylase beta subunit of Streptomyces coelicolor. *Biochemistry* **49**, 7367-7376 (2010).
17. J. J. Hu *et al.*, Discovery, structure, and function of filamentous 3-methylcrotonyl-CoA carboxylase. *Structure* **31**, 100-110 e104 (2023).
18. J. K. J. Lee *et al.*, CryoEM reveals oligomeric isomers of a multienzyme complex and assembly mechanics. *J Struct Biol X* **7**, 100088 (2023).
19. F. Kalousek, M. D. Darigo, L. E. Rosenberg, Isolation and characterization of propionyl-CoA carboxylase from normal human liver. Evidence for a protomeric tetramer of nonidentical subunits. *J Biol Chem* **255**, 60-65 (1980).
20. J. Wei, L. Tong, Crystal structure of the 500-kDa yeast acetyl-CoA carboxylase holoenzyme dimer. *Nature* **526**, 723-727 (2015).
21. S. Xiang, L. Tong, Crystal structures of human and Staphylococcus aureus pyruvate carboxylase and molecular insights into the carboxyltransfer reaction. *Nat Struct Mol Biol* **15**, 295-302 (2008).

389 22. S. Q. Zheng *et al.*, MotionCor2: anisotropic correction of beam-induced motion for
390 improved cryo-electron microscopy. *Nat Methods* **14**, 331-332 (2017).
391 23. T. Grant, N. Grigorieff, Measuring the optimal exposure for single particle cryo-EM using
392 a 2.6 A reconstruction of rotavirus VP6. *Elife* **4**, e06980 (2015).
393 24. A. Punjani, J. L. Rubinstein, D. J. Fleet, M. A. Brubaker, cryoSPARC: algorithms for rapid
394 unsupervised cryo-EM structure determination. *Nat Methods* **14**, 290-296 (2017).
395 25. E. F. Pettersen *et al.*, UCSF Chimera — a visualization system for exploratory research and
396 analysis. *J Comput Chem* **25**, 1605-1612 (2004).
397 26. S. Chen *et al.*, High-resolution noise substitution to measure overfitting and validate
398 resolution in 3D structure determination by single particle electron cryomicroscopy.
399 *Ultramicroscopy* **135**, 24-35 (2013).
400 27. J. Jumper *et al.*, Highly accurate protein structure prediction with AlphaFold. *Nature* **596**,
401 583-589 (2021).
402 28. M. Hunkeler *et al.*, Structural basis for regulation of human acetyl-CoA carboxylase. *Nature*
403 **558**, 470-474 (2018).
404 29. R. F. Alford *et al.*, The Rosetta All-Atom Energy Function for Macromolecular Modeling
405 and Design. *J Chem Theory Comput* **13**, 3031-3048 (2017).
406 30. P. Emsley, B. Lohkamp, W. G. Scott, K. Cowtan, Features and development of Coot. *Acta*
407 *Crystallogr D Biol Crystallogr* **66**, 486-501 (2010).
408 31. P. D. Adams *et al.*, PHENIX: a comprehensive Python-based system for macromolecular
409 structure solution. *Acta Crystallogr D Biol Crystallogr* **66**, 213-221 (2010).
410

Acknowledgments
We thank Drs. Xiaofeng Zhang and Xiechao Zhan for valuable discussion and suggestions on structure determination. We thank the Cryo-EM Facility, the High-Performance Computing Center, and the Mass Spectrometry & Metabolomics Core Facility of Westlake University for technical support.

Funding:

"Pioneer" and "Leading Goose" R&D Program of Zhejiang 2024SSYS0036 (Q.H.)

Westlake Laboratory of Life Sciences and Biomedicine (Q.H.)

Westlake Education Foundation (Q.H.)

Author contributions:

Conceptualization: Q.H., F.Z.

Methodology: Q.H., F.Z.

Investigation: F.Z., Y.Zhang, Y.Zhu

Visualization: F.Z., Y.Zhang

Funding acquisition: Q.H.

Project administration: Q.H., F.Z.

Supervision: Q.H., Y.S.

Writing – original draft: Q.H., F.Z.

Writing – review & editing: Q.H., Y.S., Q.Z.

Competing interests: Authors declare that they have no competing interests.

Data and materials availability: The cryo-EM structures have been deposited in the Protein Data Bank with the accession codes 8XL3 (PCC-apo), 8XL4 (PCC-ACO), 8XL5 (PCC-PCO), 8XL6 (MCC-apo), 8XL7 (MCC-ACO) and 8XL8 (MCC-PCO). The cryo-EM maps have been deposited in the Electron Microscopy Data Bank with the accession codes EMD-38436 (PCC-apo), EMD-38437 (PCC-ACO), EMD-38438 (PCC-PCO), EMD-38439 (MCC-apo), EMD-38440 (MCC-ACO) and EMD-38441 (MCC-PCO). The predicted structures of human PCC and MCC subunits used for cryo-EM model building were downloaded from the AlphaFold Protein Structure Database with the accession codes AF-P05165-F1 (PCCα), AF-P05166-F1 (PCCβ), AF-Q96RQ3-F1 (MCCα) and AF-Q9HCC0-F1 (MCCβ). The structures of bacteria PCC (PDB codes: 1XNY, 3N6R, 6YBP) and MCC (PDB codes: 3U9S and 3U9T) were used for structural analysis in this study.

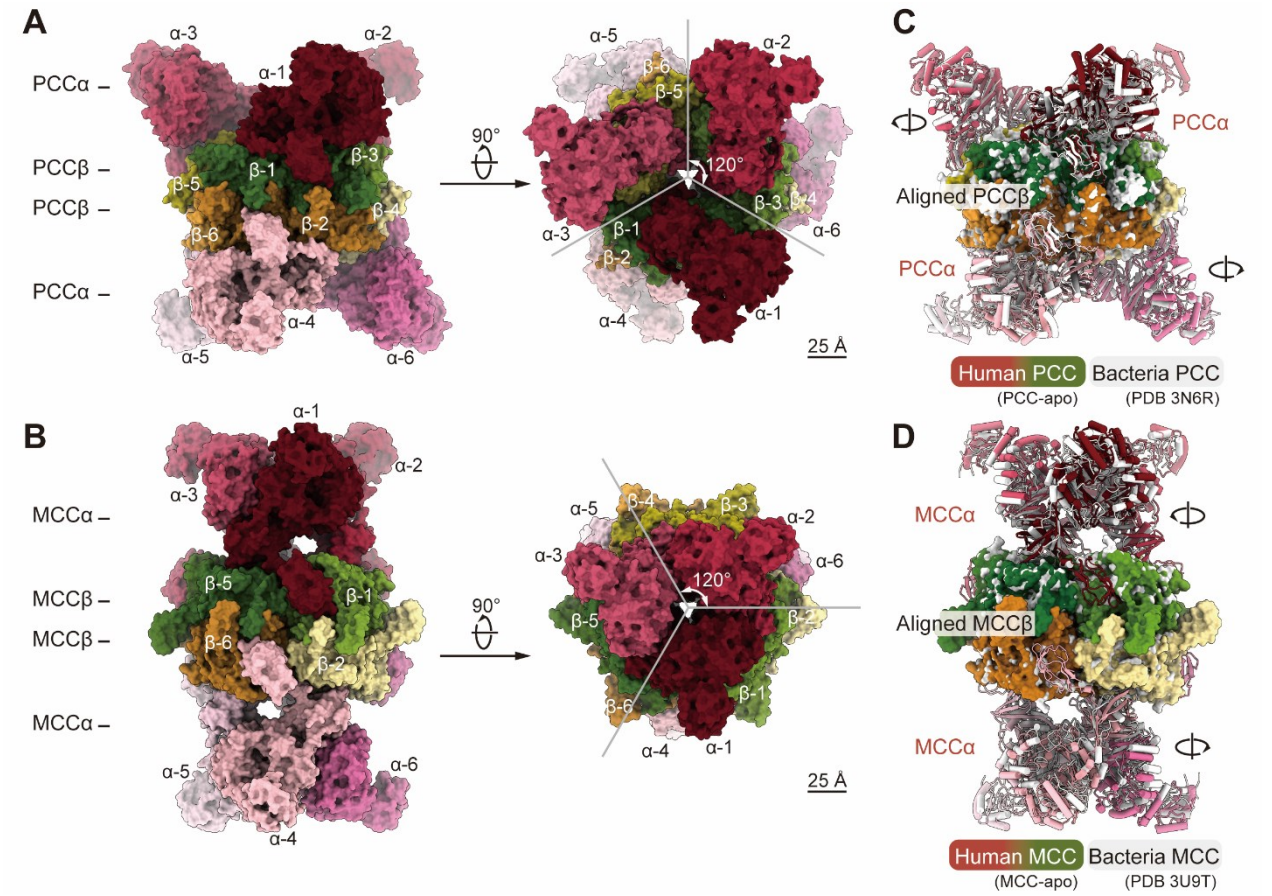

Fig. 1. The overall structures of human PCC and MCC holoenzymes. (**A, B**) The side view (left) and top view (right) of human PCC holoenzyme (PCC-apo) (**A**) and MCC holoenzyme (MCC-apo) (**B**). Both holoenzymes are dodecamers consisting of six α subunits and six β subunits. (**C**) Alignment of the PCCβ core in human PCC holoenzyme (PCC-apo) with that in a bacteria PCC holoenzyme (PDB code: 3N6R)(*12*). (**D**) Alignment of the MCCβ core in human MCC holoenzyme (MCC-apo) with that in a bacteria MCC holoenzyme (PDB code: 3U9T)(*13*). The β subunit cores in human PCC and MCC holoenzymes closely resemble their bacterial homologs, whereas the α subunits exhibit slightly different orientations in comparison to their bacterial homologs.

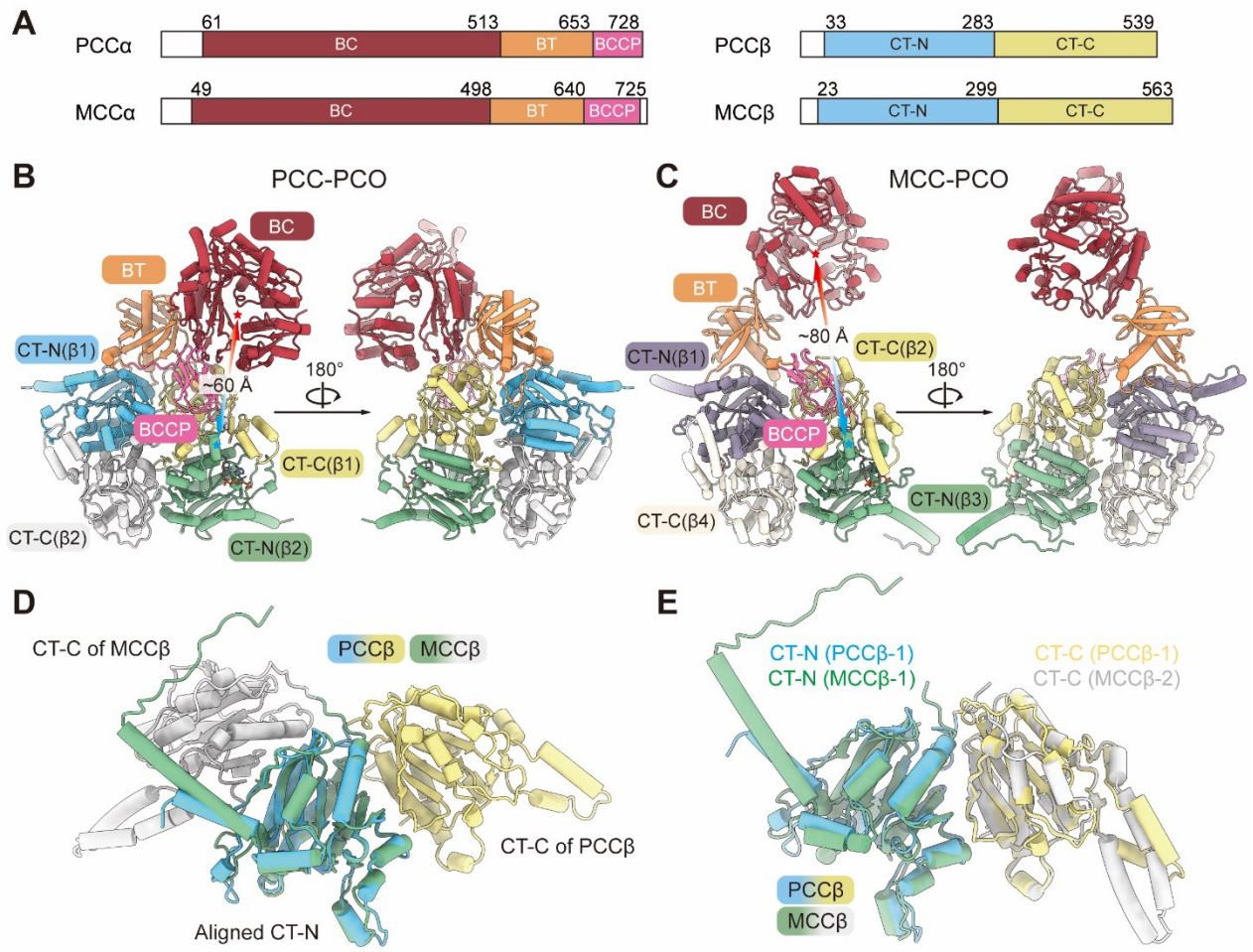

Fig. 2. Domain organization of human PCC and MCC holoenzymes. (**A**) Schematic illustration of the domain organization of human PCC (top) and MCC (bottom). Both PCC and MCC consist of α and β subunits. From the N-terminal to the C-terminal, each α subunit contains a BC (red), a BT (orange), and a BCCP (pink) domain. Each β subunit contains a CT domain, which can be divided into the CT-N (blue) and CT-C (yellow) subdomains. (**B, C**) Organization of the catalytic domains in the propionyl-CoA-bound PCC holoenzyme (PCC-PCO) (**B**) and MCC holoenzyme (**C**). (**D**) Alignment of the CT-N subdomain of PCCβ with that of MCCβ shows the different arrangement of the CT domains in human PCC and MCC. (**E**) One PCCβ subunit aligns well with the CT-N and CT-C subdomains from two adjacent MCCβ subunits in the MCC holoenzyme.

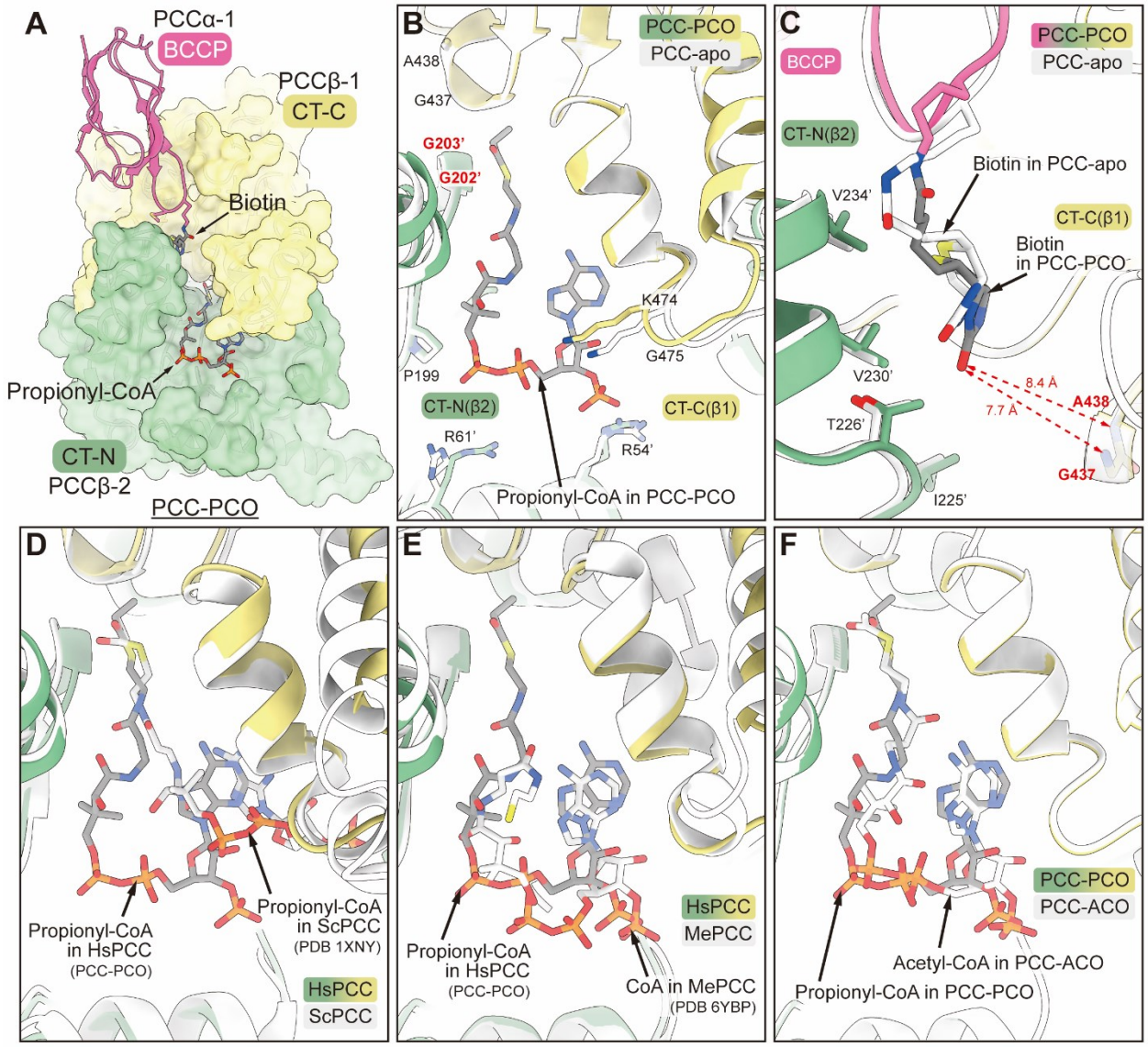

Fig. 3. Acyl-CoA binding in human PCC holoenzyme. (**A**) Surface representation of the binding pockets of biotin and propionyl-CoA in the PCC-PCO structure. (**B, C**) Alignment of the CT-N subdomain in the PCC-PCO structure with that in the PCC-apo structure. Slight conformational changes of the acyl-CoA binding pocket upon propionyl-CoA binding were observed (**B**), and the AMKM motif and biotin covalently linked to it show minor conformational differences (**C**). The distances between the carbonyl oxygen in the ureido ring of the biotin and the main chain amide of the catalytic residues G437 and A438 in the PCC-PCO structure are 7.7 Å and 8.4 Å, respectively. (**D**) Alignment of the CT-N subdomain in the PCC-PCO structure with that in the ScPCC structure (PDB code: 1XNY)(*14*). The propionyl-CoA in the two structures has distinct binding modes. (**E**) Alignment of the CT-N subunit in the PCC-PCO structure with that in the MePCC structure (PDB code: 6YBP)(*15*). The propionyl-CoA binds at the similar positions in both structures. (**F**) Alignment of the CT-N subunit in the PCC-PCO structure with that in the PCC-ACO structure. The propionyl-CoA and acetyl-CoA in the two structures show highly similar binding modes.

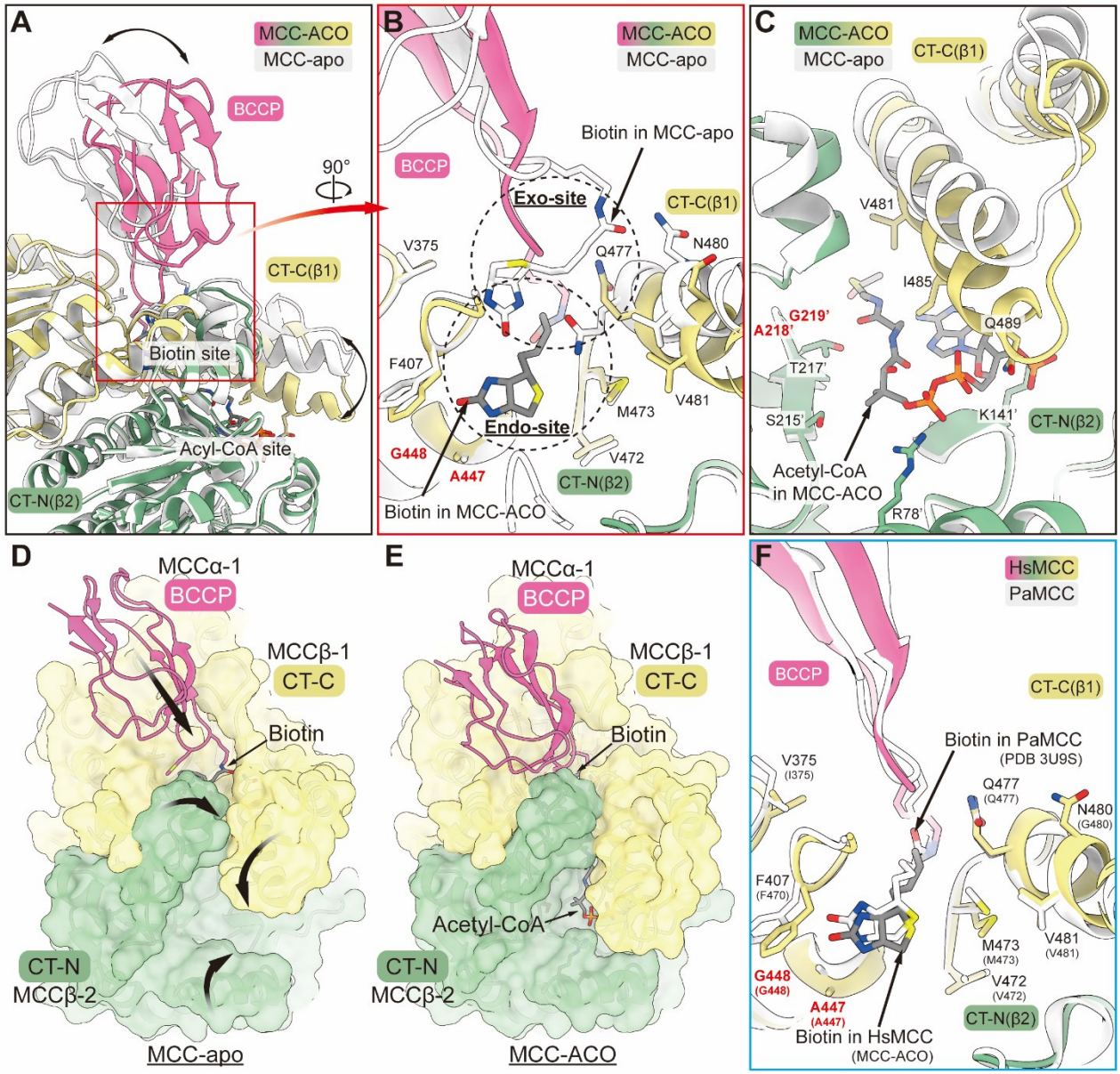

Fig. 4. Conformational changes of human MCC holoenzyme upon acetyl-CoA binding. (**A**–**C**) Alignment of the CT-N subdomain in the MCC-ACO structure with that in the MCC-apo structure. The BCCP domain moves towards the CT-C subdomain in the MCC-ACO structure compared to that in the MCC-apo structure (**A**). The covalently linked biotin binds to an exo-site in the MCC-apo structure but relocates to an endo-site that is closer to the catalytic residues A447 and G448 (see fig. S10) in the MCC-ACO structure (**B**). The helices around the acyl-CoA binding pocket show conformational differences in the MCC-ACO structure compared to that in the MCC-apo structure (**C**). (**D**, **E**) Surface representation of the binding pockets of biotin and acyl-CoA in the structures of MCC-apo and MCC-ACO. The acyl-CoA binding pocket adopts an open conformation in the MCC-apo structure (**D**) but switches to a close conformation in the MCC-ACO structure (**E**). (**F**) Alignment of the CT-N subdomain in the MCC-ACO structure with that in the PaMCC structure (PDB code: 3U9S)(*13*). The covalently linked biotin and its binding pocket adopt similar conformation in the two structures.

Supplementary Materials

Figs. S1 to S10
Tables S1 and S2

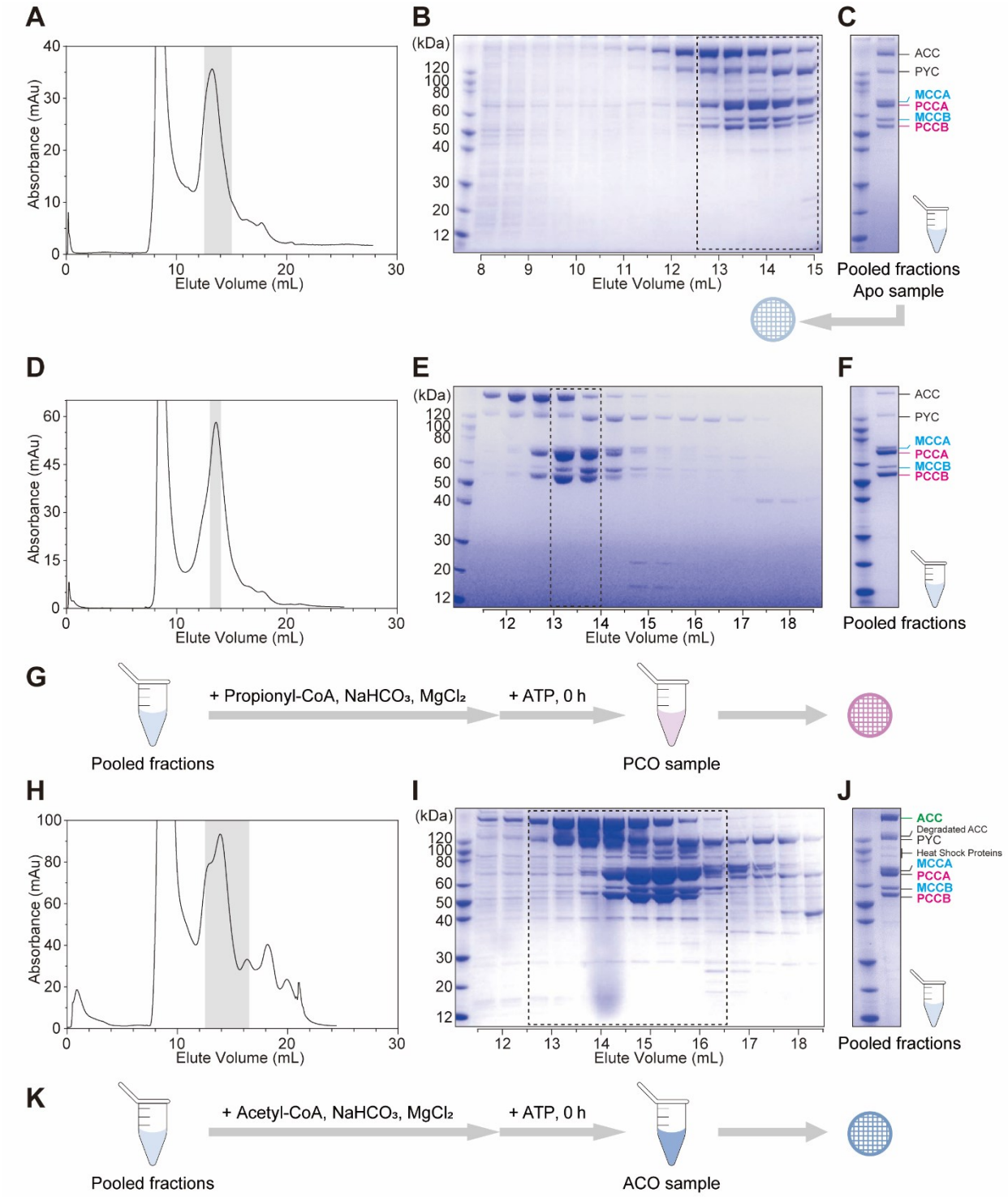

Fig. S1. Protein purification and cryo-EM sample preparation. (**A**–**C**) Preparation of the apo sample. The proteins eluted from Strep-Tactin®XT resin was further purified by size-exclusion chromatography (**A**). The fractions were analyzed by SDS-PAGE and visualized by Coomassie blue staining (**B**). The peak fractions were combined and analyzed by mass spectrometry, and the concentrated sample was directly frozen on a Holey Carbon filmed 300-mesh gold grid (Quantifoil) (**C**). (**D**–**G**) Preparation of the PCO sample. The proteins eluted from Strep-Tactin®XT resin was further purified by size-exclusion chromatography (**D**). The fractions were analyzed by SDS-PAGE and visualized by Coomassie blue staining (**E**). The peak fractions were combined and analyzed by mass spectrometry (**F**). The purified proteins were concentrated and incubated with propionyl-CoA,

507 $NaHCO_3$ and $MgCl_2$, and mixed with ATP before frozen on a Holey Carbon filmed 300-mesh gold
508 grid (Quantifoil) (**G**). (**H**–**K**) Preparation of the ACO sample. The proteins eluted from Strep-
509 Tactin®XT resin was further purified by size-exclusion chromatography (**H**). The fractions were
510 analyzed by SDS-PAGE and visualized by Coomassie blue staining (**I**). The peak fractions were
511 combined and analyzed by mass spectrometry (**J**). The purified proteins were concentrated and
512 incubated with acetyl-CoA, $NaHCO_3$ and $MgCl_2$, and mixed with ATP before frozen on a Holey
513 Carbon filmed 300-mesh gold grid (Quantifoil) (**K**).

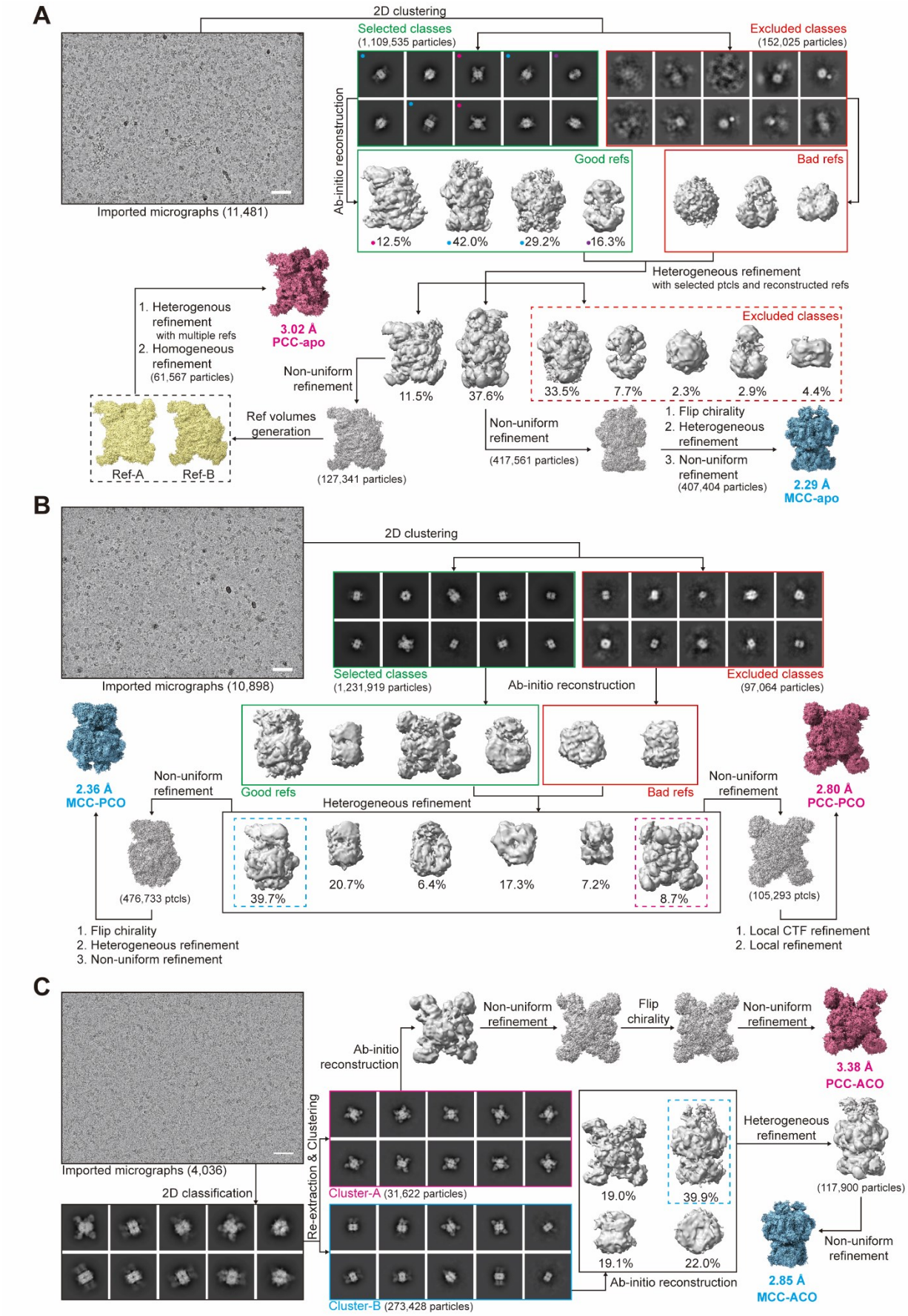

Fig. S2. Flowchart for the cryo-EM data processing of human PCC and MCC holoenzymes. (**A**) Cryo-EM data processing of the PCC-apo and MCC-apo structures. Particles from 11,481

517 micrographs went through multiple rounds of classification to reconstruct several cryo-EM density
518 maps. The final cryo-EM density maps achieved the resolutions of 3.02 Å and 2.29 Å for PCC-apo
519 and MCC-apo, respectively. For the 2D classes and 3D volumes, the red dots indicate PCC, and the
520 blue dots indicate MCC. (**B**) Cryo-EM data processing of the PCC-PCO and MCC-PCO structures.
521 Particles from 10,898 micrographs went through multiple rounds of classification to reconstruct
522 several cryo-EM density maps. The final cryo-EM density maps achieved the resolutions of 2.80 Å
523 and 2.36 Å for PCC-PCO and MCC-PCO, respectively. (**C**) Cryo-EM data processing of the PCC-
524 ACO and MCC-ACO structures. Particles from 4,036 micrographs went through multiple rounds
525 of classification to reconstruct several cryo-EM density maps. The final cryo-EM density maps
526 achieved the resolutions of 3.38 Å and 2.85 Å for PCC-ACO and MCC-ACO, respectively. The
527 scale bar in each micrograph is 50 nm.

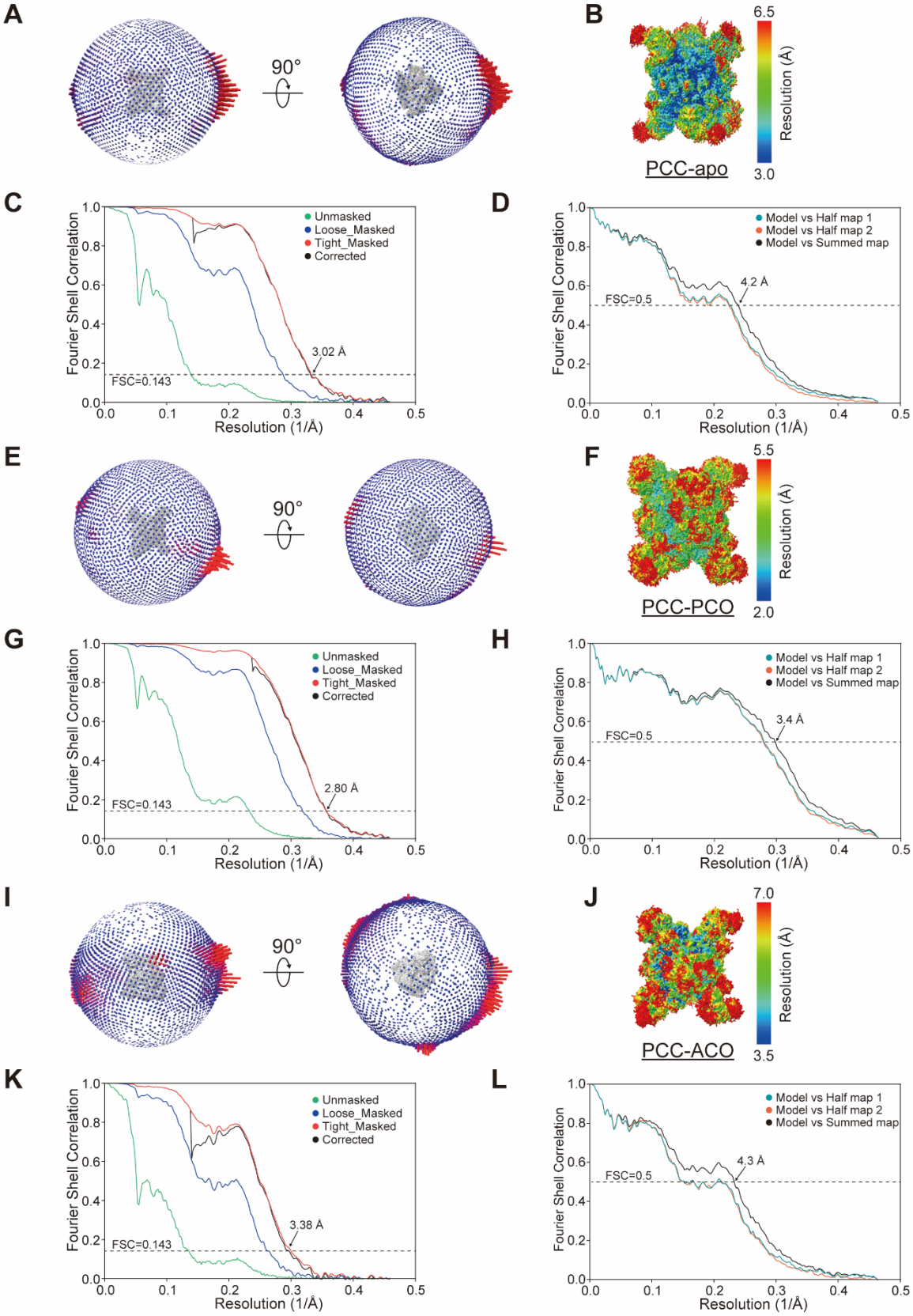

Fig. S3. Cryo-EM analysis of human PCC holoenzymes. (**A**–**D**) Cryo-EM analysis of the PCC-apo structure. (**A**) Cryo-EM map and the corresponding Euler distribution plot of the PCC-apo structure. (**B**) The local resolution estimation of the PCC-apo structure. (**C**) The gold standard FSC curves and (**D**) the FSC curves for cross-validation of the PCC-apo structure. (**E**–**H**) Cryo-EM analysis of the PCC-PCO structure. (**E**) Cryo-EM map and the corresponding Euler distribution

plot of the PCC-PCO structure. (**F**) The local resolution estimation of the PCC-PCO structure. (**G**) The gold standard FSC curves and (**H**) the FSC curves for cross-validation of the PCC-PCO structure. (**I**–**L**) Cryo-EM analysis of the PCC-ACO structure. (**I**) Cryo-EM map and the corresponding Euler distribution plot of the PCC-ACO structure. (**J**) The local resolution estimation of the PCC-ACO structure. (**K**) The gold standard FSC curves and (**L**) the FSC curves for cross-validation of the PCC-ACO structure. The particles were extracted with a box size of 488 pixels. The map resolution was determined by the reciprocal of the spatial frequency at FSC = 0.143, and the consistency of the structure optimization process was verified by comparison of the molecular model with the summed (the black curves) or half (the red or green curves) maps at FSC = 0.5(*26, 31*).

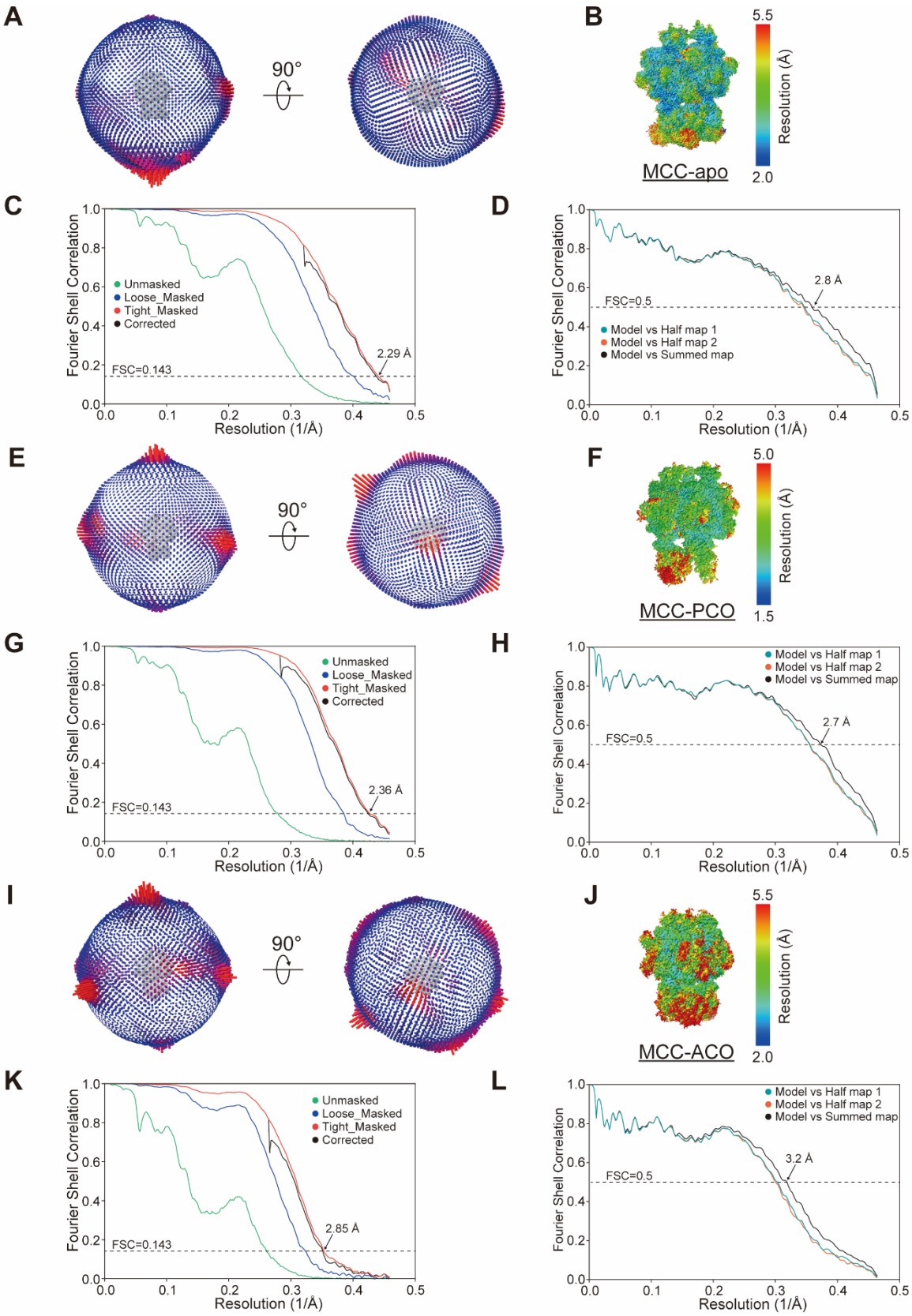

Fig. S4. Cryo-EM analysis of human MCC holoenzymes. (**A**–**D**) Cryo-EM analysis of the MCC-apo structure. (**A**) Cryo-EM map and the corresponding Euler distribution plot of the MCC-apo structure. (**B**) The local resolution estimation of the MCC-apo structure. (**C**) The gold standard FSC curves and (**D**) the FSC curves for cross-validation of the MCC-apo structure. (**E**–**H**) Cryo-EM analysis of the MCC-PCO structure. (**E**) Cryo-EM map and the corresponding Euler distribution

plot of the MCC-PCO structure. (**F**) The local resolution estimation of the MCC-PCO structure. (**G**) The gold standard FSC curves and (**H**) the FSC curves for cross-validation of the MCC-PCO structure. (**I**–**L**) Cryo-EM analysis of the MCC-ACO structure. (**I**) Cryo-EM map and the corresponding Euler distribution plot of the MCC-ACO structure. (**J**) The local resolution estimation of the MCC-ACO structure. (**K**) The gold standard FSC curves and (**L**) the FSC curves for cross-validation of the MCC-ACO structure. The particles were extracted with a box size of 488 pixels. The map resolution was determined by the reciprocal of the spatial frequency at FSC = 0.143, and the consistency of the structure optimization process was verified by comparison of the molecular model with the summed (the black curves) or half (the red or green curves) maps at FSC = 0.5(*26, 31*).

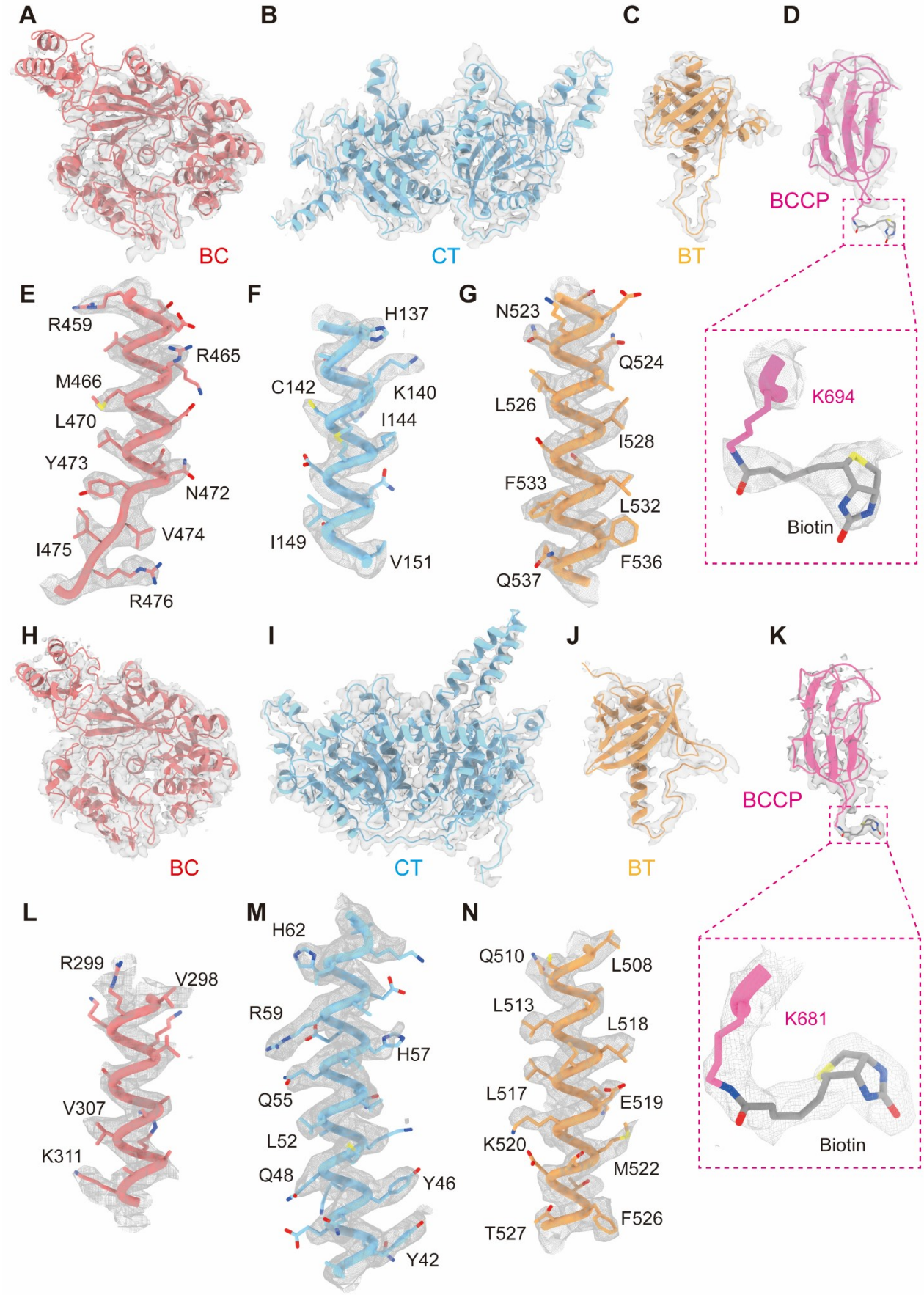

Fig. S5. The local density of human PCC and MCC holoenzymes. (**A**–**D**) Cryo-EM maps of the BC domain (**A**), CT domain (**B**), BT domain (**C**) and biotinylated BCCP domain (**D**) in the PCC-

apo structure. The biotin is covalently linked to K694 at the AMKM motif of the BCCP domain (**D**). (**E**–**G**) Cryo-EM maps of representative α-helices in the BC (**E**), CT (**F**) and BT (**G**) domains in the PCC-apo structure. (**H**–**K**) Cryo-EM maps of the BC domain (**H**), CT domain (**I**), BT domain (**J**) and biotinylated BCCP domain (**K**) in the MCC-apo structure. The biotin is covalently linked to K681 at the AMKM motif of the BCCP domain (**K**). (**L**–**N**) Cryo-EM maps of representative α-helices in the BC (**L**), CT (**M**) and BT (**N**) domains in the MCC-apo structure.

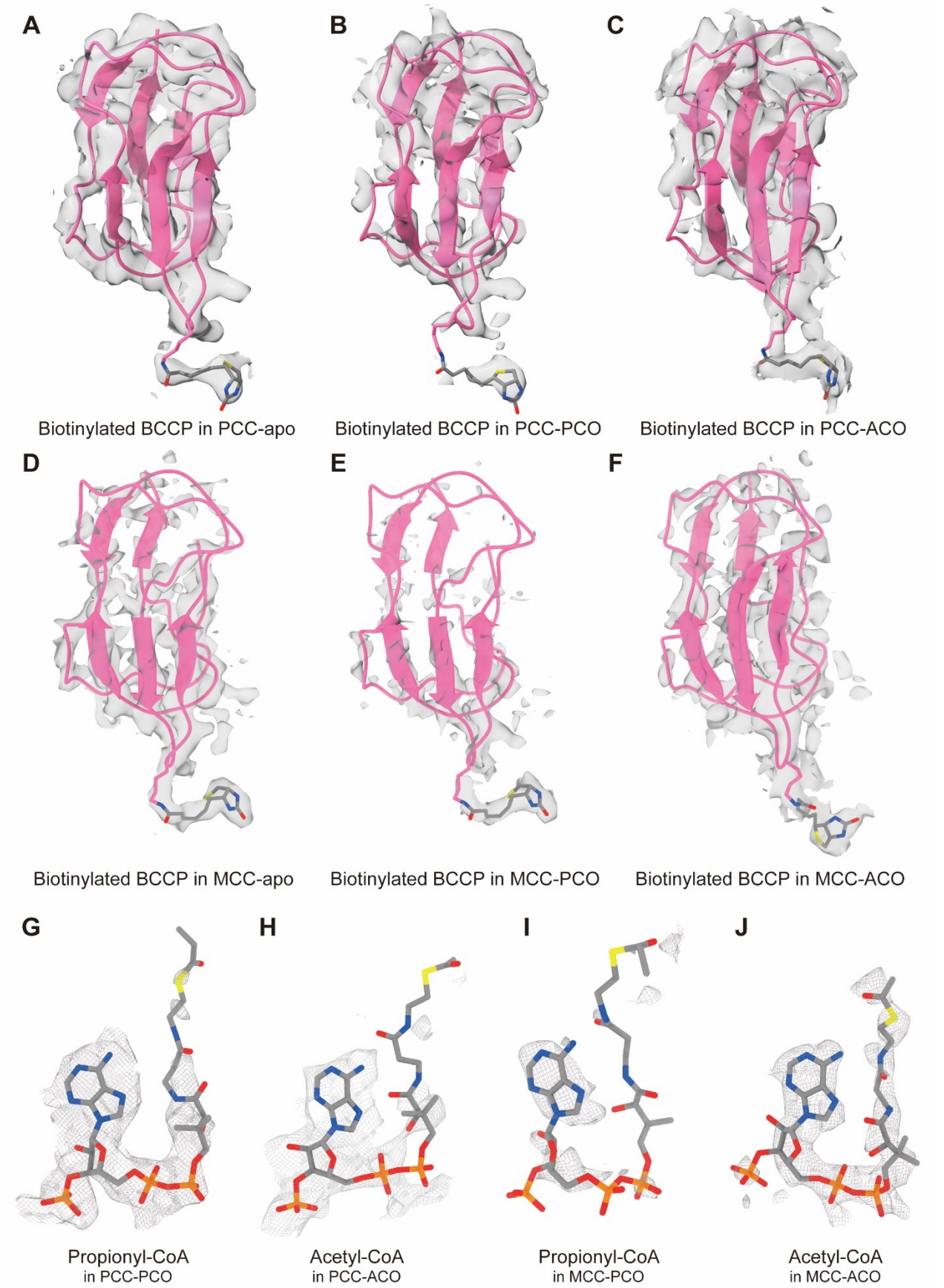

Fig. S6. The local density of the biotinylated BCCP domains and acyl-CoA in human PCC and MCC holoenzymes. (**A**–**C**) Cryo-EM maps of the biotinylated BCCP in the PCC-apo (**A**),

PCC-PCO (**B**) and PCC-ACO (**C**) structures. (**D**–**F**) Cryo-EM maps of the biotinylated BCCP in the MCC-apo (**D**), MCC-PCO (**E**) and MCC-ACO (**F**) structures. (**G**–**J**) Cryo-EM maps of the propionyl-CoA in the PCC-PCO structure (**G**), the acetyl-CoA in the PCC-ACO structure (**H**), the propionyl-CoA in the MCC-PCO structure (**I**) and the acetyl-CoA in the MCC-ACO structure (**J**). The cryo-EM maps were displayed at a RMS level of 5 for (**A**–**F**) and of 4.5 for (**G**–**J**).

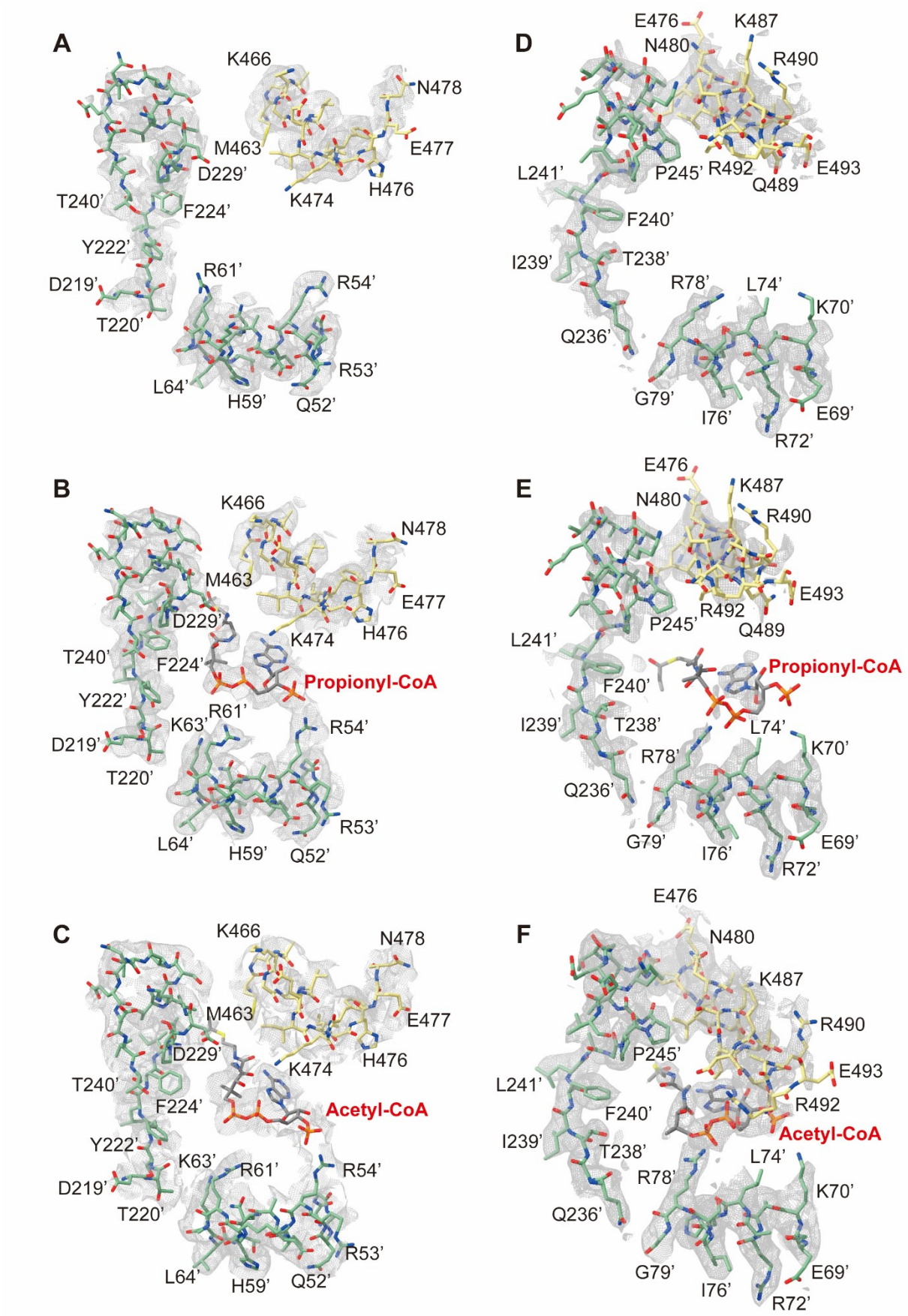

Fig. S7. The local density of the acyl-CoA binding pocket in human PCC and MCC holoenzymes. (**A**–**C**) Cryo-EM maps of the acyl-CoA binding pocket in the PCC-apo (**A**), PCC-

580 PCO (**B**) and PCC-ACO (**C**) structures. (**D**–**F**) Cryo-EM maps of the acyl-CoA binding pocket in
581 the MCC-apo (**D**), PCC-PCO (**E**) and PCC-ACO (**F**) structures. All cryo-EM maps were displayed
582 at an RMS level of 4.5.

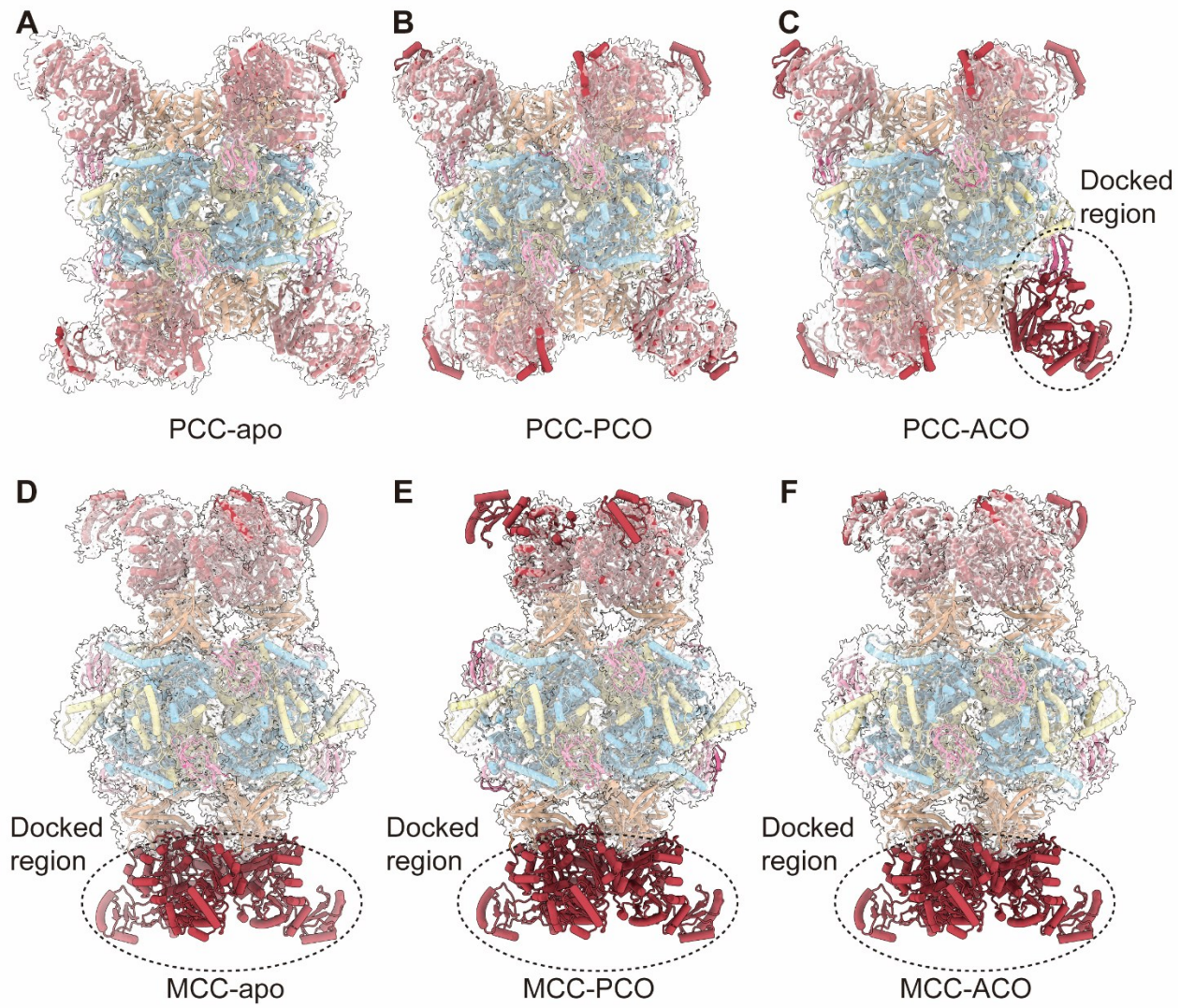

Fig. S8. The Cryo-EM maps of human PCC and MCC holoenzymes. Fig. S8. The Cryo-EM maps of human PCC and MCC holoenzymes. (**A**–**C**) Cryo-EM maps for the PCC-apo (RMS Level = 2.8 σ) (**A**), PCC-PCO (RMS Level = 2.7 σ) (**B**) and PCC-ACO (RMS Level = 3.5 σ) (**C**). The cryo-EM maps are displayed in semitransparent white color and superimposed with the corresponding stereo models. The density of one PCCα subunit in the PCC-ACO structure is partially missing (indicated by dashed circle in panel **C**). (**D**–**F**) Cryo-EM maps for the MCC-apo (RMS Level = 2.3 σ) (**D**), MCC-PCO (RMS Level = 2.0 σ) (**E**) and MCC-ACO (RMS Level= 2.8 σ) (**F**). The density of three MCCα subunits in each MCC holoenzyme structure are partially missing (indicated by dashed circles in panels **D**–**F**).

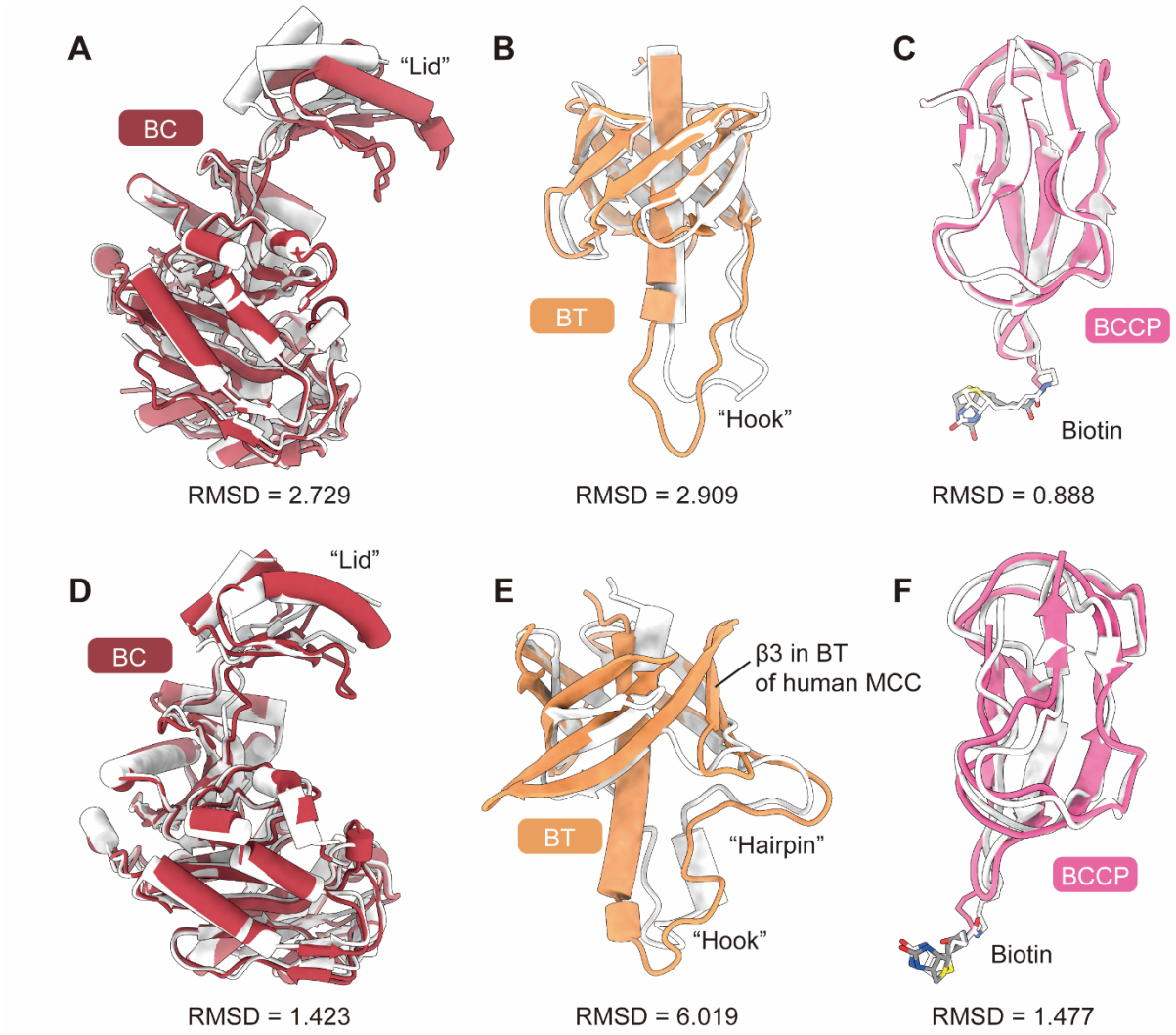

Fig. S9. Comparison of the domain structures of human PCC and MCC with that of their bacteria homologs. (**A**–**C**) Alignments of the BC domain (**A**), BT domain (**B**) and biotinylated BCCP domain (**C**) in human PCC structure (PCC-apo) with that in a bacteria PCC structure (PDB code: 3N6R)(*12*). (**D**–**F**) Alignments of the BC domain (**D**), BT domain (**E**) and biotinylated BCCP domain (**F**) in human MCC structure (MCC-apo) with that in a bacteria MCC structure (PDB code: 3U9T)(*13*).

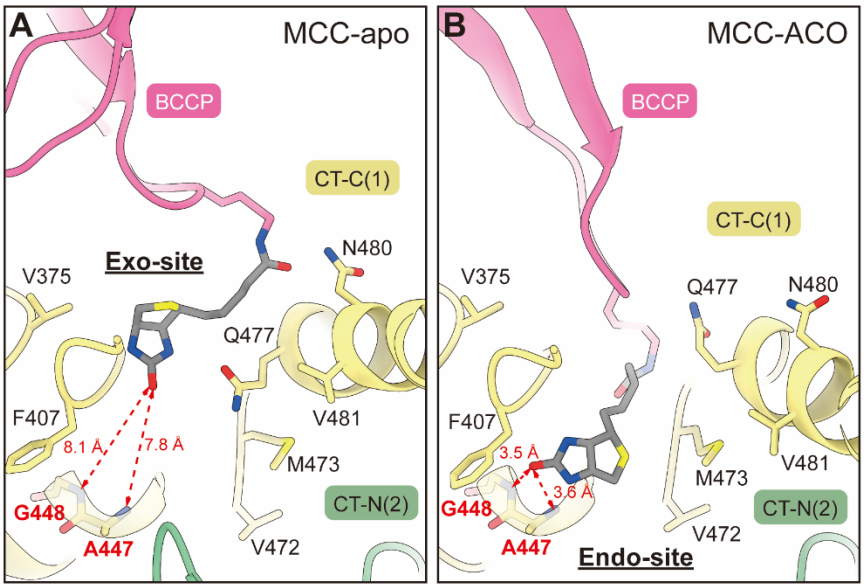

Fig. S10. The biotin binding sites in the structures of human MCC holoenzyme. (**A**) The covalently linked biotin in the MCC-apo structure binds to a site distant from the catalytic residues in the CT domain. This site is thus referred to as the exo-site. The distances between the carbonyl oxygen of the ureido ring of biotin and the main chain nitrogen atoms of the catalytic residues A447 and G448 in the CT domain are 7.8 Å and 8.1 Å, respectively. (**B**) The covalently linked biotin in the MCC-ACO structure moves to a site closer to the catalytic residues A447 and G448 in the CT domain. This site is referred to as the endo-site. The distances between the carbonyl oxygen of the ureido ring of biotin and the main chain nitrogen atoms of the catalytic residues A447 and G448 in the CT domain are shortened to 3.6 Å and 3.5 Å, respectively.

610 **Table S1. Cryo-EM data collection, reconstruction, refinement, and validation statistics of**
611 **human PCC structures.**

Sample	**PCC-apo**	**PCC-ACO**	**PCC-PCO**
PDB code	8XL3	8XL4	8XL5
EMDB code	EMD-38436	EMD-38437	EMD-38438
		Data collection	
EM equipment		Titan Krios (Thermo Fisher Scientific)	
Voltage (kV)		300	
Detector		Gatan K3 Summit	
Energy filter		Gatan GIF Quantum, 20 eV slit	
Pixel size (Å)		1.0773	
Electron dose (e^-/Å^2)		50	
Defocus range (μm)		−1.2 to −2.2	
Number of collected micrographs	11,481	4,036	10,898
		3D Reconstruction	
SoftwaresSoftware		cryoSPARC 3.3.2	
Number of used particles	61,567	30,932	105,293
Resolution (Å)	3.02	3.38	2.80
Symmetry		C1	
Map sharpening B-factor (Å^2)	68	70.3	75.8
		Refinement	
Software		Phenix 1.14	
Cell dimensions			
a=b=c (Å)	525.7224	517.104	525.7224
$\alpha=\beta=\gamma$ (˚)		90	
Model composition			
Protein residues	7,050	6,521	7,050
Side chains assigned	7,050	6,521	7,050
Biotin	6	5	6
Acetyl-CoA	0	6	0
Propionyl-CoA	0	0	6
R.m.s deviations			
Bonds length (Å)	0.010	0.010	0.010
Bonds Angle (˚)	1.064	1.008	1.041
Ramachandran plot statistics (%)			
Preferred	96.58	96.55	96.43
Allowed	2.82	2.72	2.92
Outlier	0.60	0.72	0.65

612

613 **Table S2. Cryo-EM data collection, reconstruction, refinement, and validation statistics of**
614 **human MCC structures.**

Sample	**MCC-apo**	**MCC-ACO**	**MCC-PCO**
PDB code	8XL6	8XL7	8XL8
EMDB code	EMD-38439	EMD-38440	EMD-38441
	Data collection		
EM equipment	Titan Krios (Thermo Fisher Scientific)		
Voltage (kV)	300		
Detector	Gatan K3 Summit		
Energy filter	Gatan GIF Quantum, 20 eV slit		
Pixel size (Å)	1.0773		
Electron dose (e^-/Å^2)	50		
Defocus range (μm)	−1.2 to −2.2		
Number of collected micrographs	11,481	4,036	10,898
3D Reconstruction			
Software	cryoSPARC 3.3.2		
Number of used particles	407,407	117,900	476,733
Resolution (Å)	2.29	2.85	2.36
Symmetry	C1		
Map sharpening B-factor (Å^2)	69.9	88.4	75.7
Refinement			
Software	Phenix 1.14		
Cell dimensions			
a=b=c (Å)	525.7224	517.104	525.7224
$\alpha=\beta=\gamma$ (˚)	90		
Model composition			
Protein residues	5,780	5,704	5,628
Side chains assigned	5,780	5,704	5,628
Biotin	6	6	6
Acetyl-CoA	0	6	0
Propionyl-CoA	0	0	6
R.m.s deviations			
Bonds length (Å)	0.011	0.013	0.011
Bonds Angle (˚)	1.015	1.146	1.018
Ramachandran plot statistics (%)			
Preferred	95.05	93.77	94.63
Allowed	4.74	5.60	4.94
Outlier	0.21	0.64	0.43

615